Journal of Japan Association for Earthquake Engineering, Vol. 20, No. 8, 2020

MICRO-TREMOR OBSERVATION IN YANGON CITY FOCUSING ON THE MICROSEISMS

Satoshi MORIO[1], Yoshimitsu YAMADA[2] and Tomoyuki KANEKO[3]

[1] Member of JAEE, HAKUHO Architech Co., Ltd. (Visiting Professor of Chulalongkorn University), Dr. Eng. Mie, Japan, bonno51.krungtape@gmail.com
[2] General Manager of Yangon Branch Office, FUKKEN Co., Ltd. Dr. Eng. Yangon, Myanmar, yamada@fukken.co.jp
[3] Chief Engineer of Coast/Earthquake Prevention Department, FUKKEN Co., Ltd. Hiroshima, Japan, kaneko@fukken.co.jp

ABSTRACT: The Republic of the Union of Myanmar and its surrounding area is one of the earthquake-prone areas of the world. The highly active Sagaing Fault runs down the central part of the country over 1,500 km and is 30 km away on the east of Yangon, the former capital city. Meanwhile, there are many old buildings in Yangon which were built up to the mid-twentieth century during British colonial rule. Moreover, there are no seismic standards for office and commercial buildings that are being built in recent years and extensive damage is expected if an earthquake occurs. To evaluate the ground amplification function during earthquake, the authors conducted micro tremor observations at North Dagon in Yangon with consideration of short period (of around 1 s) and long period microseisms. The short and long period seisms involve with ground properties in the top several tens of meters and several hundred meters to several kilometers deep, respectively. A single-point (three components) micro-tremor observation and an array observation were carried out for determining the H/V spectrum and the dispersion curve of the Rayleigh wave, respectively. Then the findings as well as the estimation of the geological structure are discussed based on both results.

Key Words: Micro-tremor, H/V spectrum, Array observation, Deep underground structure

1. INTRODUCTION

The Republic of the Union of Myanmar (population: approx. 53 million) and its surrounding area is one of the earthquake-prone areas of the world. The subduction structure line along the border between the Indo-Australian plate and the Eurasian plate was the epicenter of the Sumatra earthquake (M9.1) of December 26, 2004. The subduction line runs to the north along the western boarder of Myanmar. Moreover, the Sagaing fault (Central Burma fault) is located about 30 km east of its largest city, Yangon (population approx. 5.2 million), and runs through the center of the country for 1500 km. The Sagaing fault is a highly active right-lateral strike-slip fault, and many earthquakes occurred along this fault in the past including six M7 or stronger earthquakes since the 20th century. Meanwhile, there are many old buildings in Yangon City, the former capital, built up to the mid-twentieth century during British colonial rule. In addition, there are no seismic standards for office and commercial buildings in reinforced

concrete or steel-frame that have been increasing since democratization. It can be said that the level of earthquake-resistant design in Myanmar is similar to that of Japan from 1939 to 1990, where $k_s = 0.2$ was set as the horizontal seismic coefficient[1)], and extensive damage is predicted if an earthquake occurs.

Yangon City is located at the confluence of two large rivers, namely, the Yangon River and the Bago River (see Fig. 1[3)]). While boring explorations[4)] up to about 50 m have been conducted at many places in Yangon City, little information is known for the underlying bedrock. In this study, the authors[2)] conducted micro-tremor observations for estimating the depth of seismic bedrock and evaluating the amplification characteristics of the ground during an earthquake. A single-point (three components) micro-tremor observation and an array observation were conducted at the Yangon Branch Office of Fukken Co., Ltd. The former measurement was used for determining the *H*/*V* spectrum and the latter observation was used for determining the dispersion curve of Rayleigh wave. Both of long-period micro-tremor (microseisms), which reflects the geological structure of several hundred meters to several kilometers deep, and the relatively short-period region of around 1 s that reflects the ground property of several tens of meters are considered. The results are discussed and compared with the case of Bangkok which shares some geological similarity with Yangon.

Fig. 1 Map of Yangon City[3)]

2. *H*/*V* SPECTRUM OBTAINED BY A SINGLE POINT (THREE COMPONENTS) MICRO-TREMOR OBSERVATION

Figure 1 shows the map of Yangon City (Township names) and the location of the Yangon Branch Office of Fukken Co., Ltd. A to G in the map indicate the downtown area, located at about 10 km south-southwest from the office. The Yangon River and the Bago River merge here and flow south for about 40 km to reach the Andaman Sea. The office is located in a residential area, and while a main road with relatively heavy traffic (Pinlon Road) is located at about 300 m from the office, the area around it is quiet and with little traffic, with only a few cars passing by during a single measurement (20 minutes) in the daytime.

The seismometer used for the observation was a 3-component servo type velocity-meter CV-374AV by Tokyo Sokushin Co., Ltd., (the flat region of frequency characteristics is 0.1 Hz-100 Hz, AD conversion is 24 bit and resolution is 25 μkine (1 kine = 1 cm/s^2)). Since the maximum velocity during the measurement in the midnight, which will be shown in Fig. 4 later, was about 1000 μkine, its accuracy was considered to be sufficient. The micro-tremor observation was conducted for one year (November 2014 to November 2015) twice a month on a weekday afternoon. The measurements during the rainy season, when torrential rain continues, were conducted after the rain stopped. Therefore, it is possible

that the groundwater level, density and *P*-wave velocity changed. Continuous measurement that lasted for at least 20 minutes was conducted each time. Three sections, each containing one minute of data with little noise determined through the visual examination of the waveform, were selected from each measurement, and the *H*/*V* spectrum was obtained from their average using Eq. (1) [5]. When this was compared to the average of 10 sections from the same data, they were nearly identical. Here, ω is the angular frequency, $C_{XX}(\omega)$, $C_{YY}(\omega)$ and $C_{ZZ}(\omega)$ are the power spectrum of NS, EW and UD components, respectively. The sampling rate was 100 Hz (data count = 6000), and the Parzen window (bandwidth: 0.2Hz) was used as the spectrum window.

$$\frac{H}{V}(\omega) = \frac{\sqrt{C_{XX}(\omega) + C_{YY}(\omega)}}{\sqrt{C_{ZZ}(\omega)}} \tag{1}$$

Figure 2 shows the monthly change of the *H*/*V* spectrum for one year. While there is a clear peak at around 1 s from late February to early May (the dry season) shown in Fig. 2(b), there is no peak in the long-period range. Meanwhile, clear peaks appeared in the long-period range between 3 s to 5 s, in addition to the peak at around 1 s, during the rainy season from late May to early August shown in Fig. 2(c). During the rainy season, waves in the Andaman Sea become high, and the result suggests the influence of the waves from the ocean. Fig. 2(a), from late November to early February, is for the dry season as in Fig. 2(b). During this time, a distinct peak is observed in the long-period region only in late December, and no clear peak was observed in any other observation days. The period from late August to early November, shown in Fig. 2(d) is the transition phase from the rainy season to the dry season. During this time, the peak in the long-period region appeared sometimes and did not appear at other times; thus, intermediate characteristics are observed between Fig. 2(b) and Fig. 2(c). Moreover, the width of the periodic band of the 1 s peaks of Fig. 2(a), Fig. 2(c) and Fig. 2(d) appear to be wider than that of Fig. 2(b). They appear to contain several peaks around 0.8 s to 1.5 s.

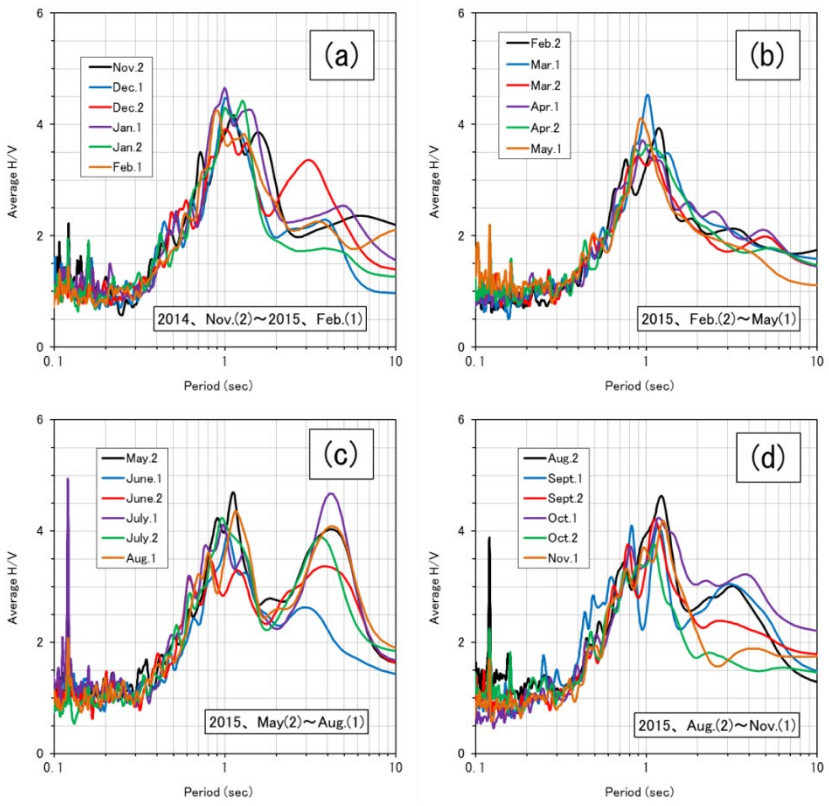

Fig. 2 Monthly change of *H*/*V* spectrum

Figure 3 compares the power spectrum of the horizontal components (numerator of Eq. (1)) and the UD component in early March, when no peak was observed in the long period, and in early August, when a clear peak was observed. The figure also contains the *H*/*V* spectrum. In early August, shown in Fig. 2(b), the power of the long-period region of the horizontal components and the UD component around 3 s to 5 s was large. It is clear that the peak of the *H*/*V* spectrum was formed by this power.

Figure 4 shows the time variation of the power spectrum of each component (NS, EW and UD) and the *H*/*V* spectrum. The measurement was conducted every four hours between nine AM and five PM. The measurement was conducted during the dry season on November 11, 2014. Similarly, to that of late December shown in Fig. 2(a), a clear peak can be seen at around 3 s to 5 s of each time slot. A peak of the power spectrum of each component (NS, EW and UD) can be seen at around 0.3 s to 0.5 s. At these peaks, the amplitude is small at 1 AM and 5 AM, and large at 9 AM and 1 PM, for every component. These differences in amplitude are about 10 times in the power spectrum. Since the amplitude increases during the time when people are active, it is inferred that these peaks around 0.3 s to 0.5 s originates from artificial vibration sources, including the cars passing by. Meanwhile, as indicated by the red circle in the graph, the difference in the amplitude of the peaks of the power spectrum of the long-period region around 3 s to 5 s between each time slot is small. From this fact, it is inferred that the source of the peaks of *H*/*V* of the long-period region is natural phenomena, including waves on the Andaman Sea and changes in atmospheric pressure, instead of human activities. Note that increase in amplitude can be observed at the long-period region of around 10 s of the power spectrum of each component. These are inferred to be the long-period noise that includes the limit of the measurement accuracy (0.1Hz-100Hz) of the seismometer.

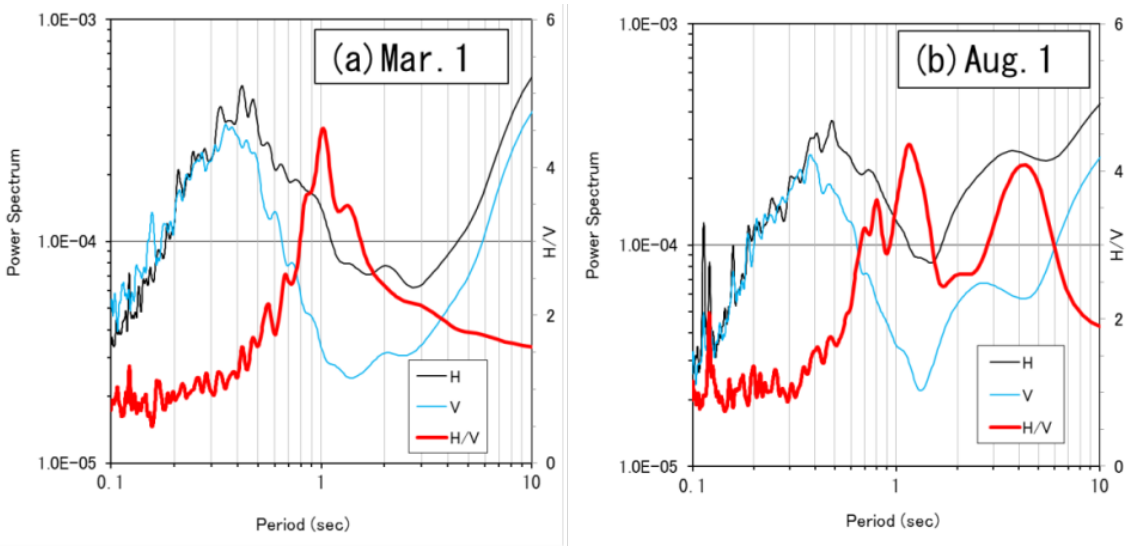

Fig. 3 Two types of typical *H*/*V* spectrum

There are many existing studies on the microseisms in Japan. Okano[6), 7)] demonstrated that the microseisms observed in the area around Kyoto are a surface wave group whose main component is the Rayleigh wave that frequently occurs off the Kii Peninsula on the Pacific Ocean side and off the Tango Peninsula on the Sea of Japan side. According to an observation over two years inside the bedrock on the Sea of Japan side, the long-period micro-tremor (microseism) is found to range between 2 s and 5 s. In addition, strong power was observed during winter from November to February, and weaker power was observed from May to August. The maximum difference between these periods was nearly two orders. Obara[9)] measured micro-tremors in many places in Japan and demonstrated that their amplitudes become gradually larger from December to January. The level of the micro-tremors increased as atmospheric pressure increased in winter, and this tendency was especially prominent on the Sea of Japan side. The temporal variation of microseisms is also observed in this study in that the power of

microseisms increases during the rainy season. This evidence suggests that microseisms are spatio-temporal. The observed data and its interpretation might be different if they are conducted over different period of time.

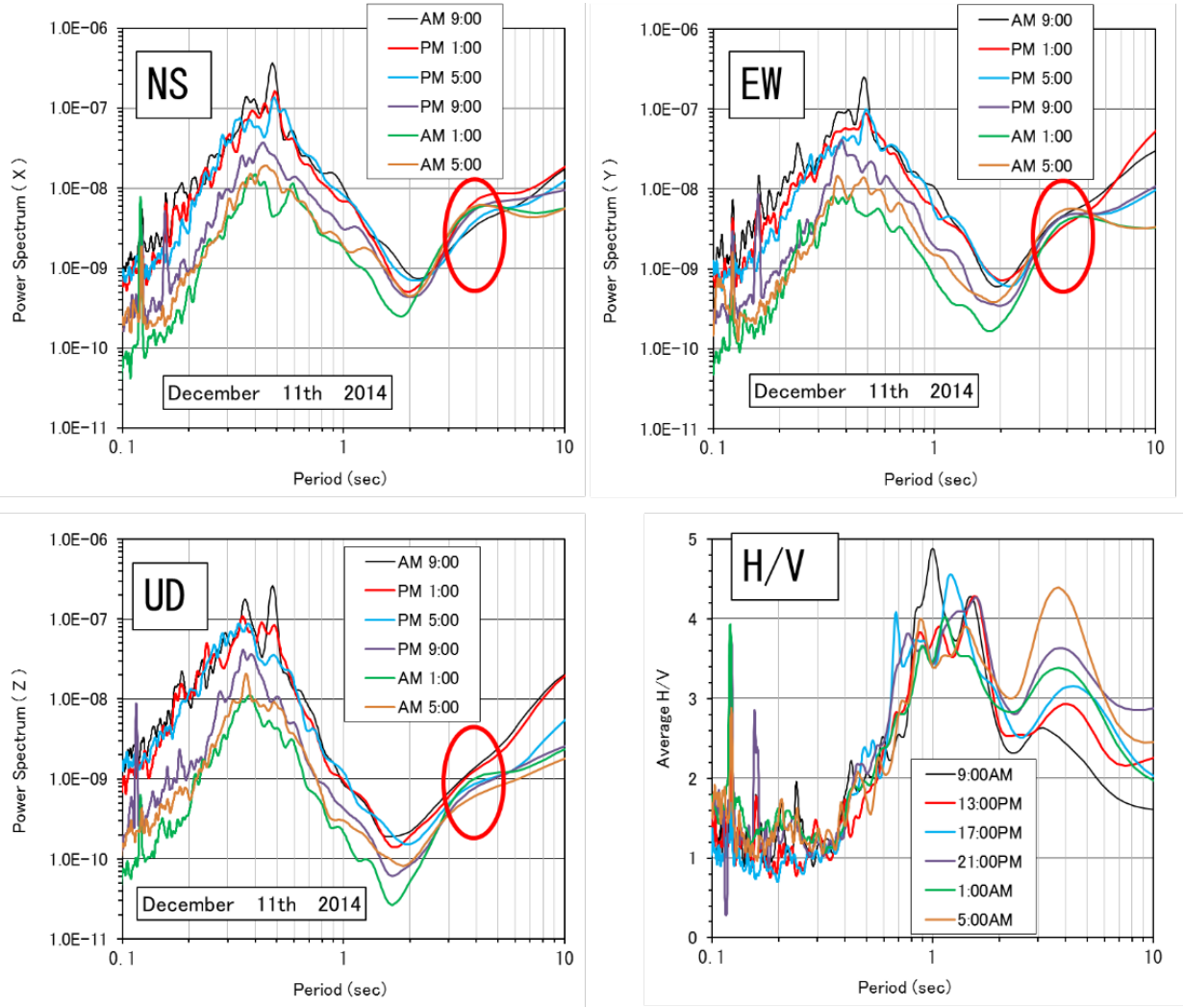

Fig. 4 Time variation of the power spectrum of each component and the *H*/*V* spectrum

3. ARRAY OBSERVATION

3.1 Circular array observation

Four seismometers (No.1～No.4), similar to those explained earlier, were used to conduct continuous array observation for 20 minutes. The location of the observation was also the same as that of Chapter 2. Ten 20 s sections with little noise were selected, and phase velocity was obtained from their average using the SPAC and CCA methods[10), 11)]. GPS was used to synchronize the seismometers, and the correlations between No. 1–No. 2, No. 1–No. 3 and No. 1–No. 4 (coherence, phase and cross correlation) were verified to be the same from a Huddle test.

Figure 5 shows the dispersion curves of phase velocity obtained through the SPAC method and the CCA method. The array radius was R = 1 m , R = 5 m and R = 10 m. From around 0.1 s to 0.4 s, nearly identical dispersion curves were obtained by both methods. However, the increase in the resolution at the long wavelength region that accompanied the increase in array radius was not particularly large. The theoretical dispersion curve is the curve of fundamental Rayleigh wave mode obtained from the

estimated underground structure. Its details are discussed later in this paper. Appendix 1 includes a comparison between the analysis result by a micro-tremor analysis program BIDO 2.0[12] and the program developed for this study. It verifies that nearly identical dispersion curves could be obtained from these two programs.

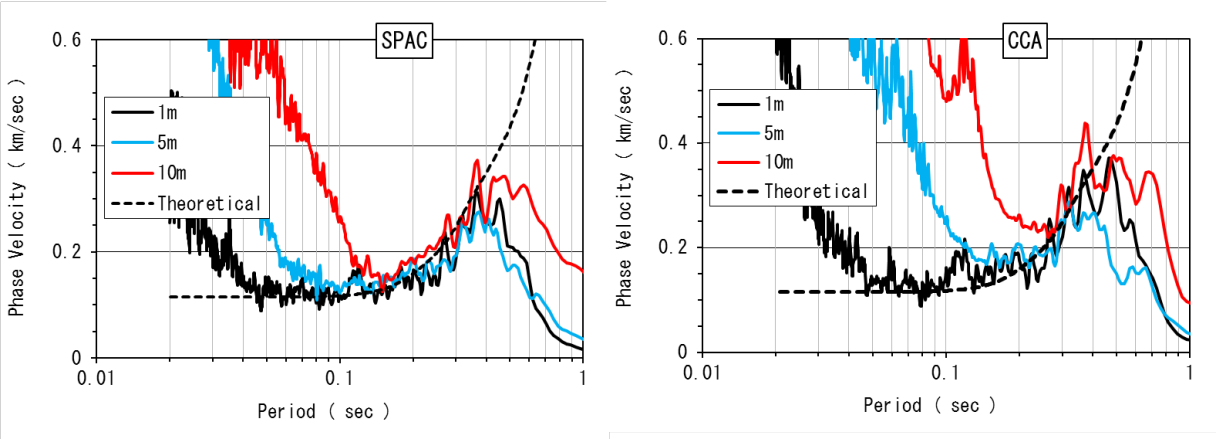

Fig. 5 Dispersion curves of phase velocity obtained through the SPAC method and the CCA method

3.2 Micro-tremor observation using the Line SPAC method

Although the micro-tremor measurement location was in a residential area, there was little traffic; radius R = 10 m was the limit for forming a circular array due to the nature of the area. Thus, two cases of micro-tremor measurement, where four seismometers were placed along the road at equal distance from each other and used for simultaneous measurement (hereafter referred to as the Line SPAC method), were conducted. The distance between each seismometer was 10 m and the extension was 30 m for Case 1, and the distance between each seismometer was 20 m and the extension was 60 m for Case 2. Aside from the fact that this Line SPAC method does not obtain the azimuthal average of coherence, this method is the same as the normal SPAC method.

Figure 6(a) shows the results of Case 1 when the distance between each seismometer was r = 10 m (No. 1–No. 2, No. 2–No. 3 and No. 3–No. 4). Similarly, Fig. 6(b) shows the result of Case 1 when the distance between each seismometer was r = 20 m (No. 1–No. 3 and No. 2–No. 4), and Fig. 6(c) shows that of Case 1 when r = 30 m (No. 1–No. 4). The thin solid line and the dotted line in the graph represent wavelength $\lambda = 2r$ and $10r$ respectively. Fig. 6(d) shows the results of Case 2 when the distance between each seismometer was r = 20 m (No. 1–No. 2, No. 2–No. 3 and No. 3–No. 4). Similarly, Fig. 6(e) shows the result of Case 2 when the distance between each seismometer was r = 40 m (No. 1–No. 3 and No. 2–No. 4), and Fig. 6(f) shows that of when r = 60 m (No. 1–No. 4). While there are some discrepancies, it appears that that within the range of $\lambda = 2r$ to $10r$, the lower limit of phase velocity mostly coincides with the theoretical dispersion curve. It is inferred that the lower limit of phase velocity corresponds with the minimum value of coherence (Eq. (18) in Ref.14). Moreover, the resolution of the long wavelength region improved as the distance between each seismometer r became larger. At r = 60 m of Case 2, the resolution of wavelength λ = 600 m ($10r$) at around 0.8 s was observed.

Regarding the azimuthal average of coherence, Yokoi and Margaryan[15] commented that “inside a city or its suburbs, there is a possibility that the azimuthal dependency of the power of micro-tremor is sufficiently mild as to conform to the theory of seismic interferometry and therefore making the azimuthal average of coherence unnecessary.” Here, analysis of Fig. 6 was conducted with an assumption that micro-tremor is uniformly transmitted from every direction within the short-period region of 1 s or less[16]. As a result, the phase velocity around 0.1 s to 0.5 s of the SPAC method and the CCA method shown in Fig. 5 and the lower limit of dispersion curve around 0.2 s to 0.9 s shown in Fig. 6 are continuous. Thus, it appears that if errors within a certain range are allowed[13), 15)], the Line SPAC method can also be used for the estimation of a dispersion curve.

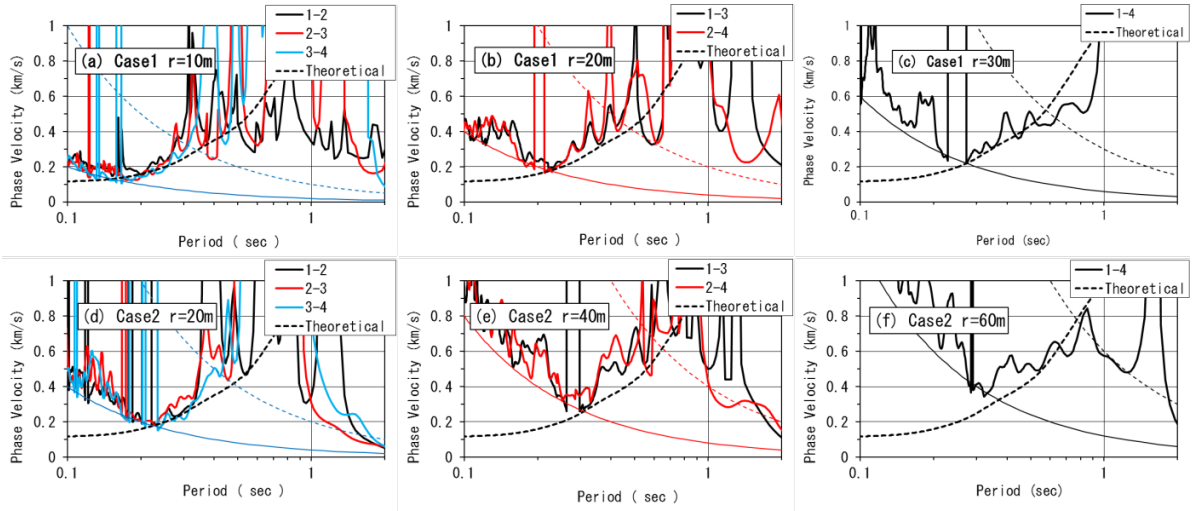

Fig. 6 Dispersion curve by Line SPAC method

4. ESTIMATION OF UNDERGROUOND STRUCTURE

4.1 Boring data up to GL−40m and estimation of deep underground structure

Three soil boring records near to the micro-tremor measurement area are shown in Fig. 7. The SPT-*N*-values were used for estimating the *S*-wave velocity *V*s. The layer with 10 or less *N*-value is clay, silty clay or clayey silt, and that with *N*-value of 10 or more is alternate layers of either sandy clay or clayey sand. For the conversion of *N*-value to *V*s, several conversion equations have been proposed in Japan. However, there is no past study on this subject in Myanmar. Thus, the following equations based on the Seismic design of the Specifications for highway bridges[17] were used.

$$Clay: V_S = 100N^{1/3} \quad (2)$$

$$Sand: V_S = 80N^{1/3} \quad (3)$$

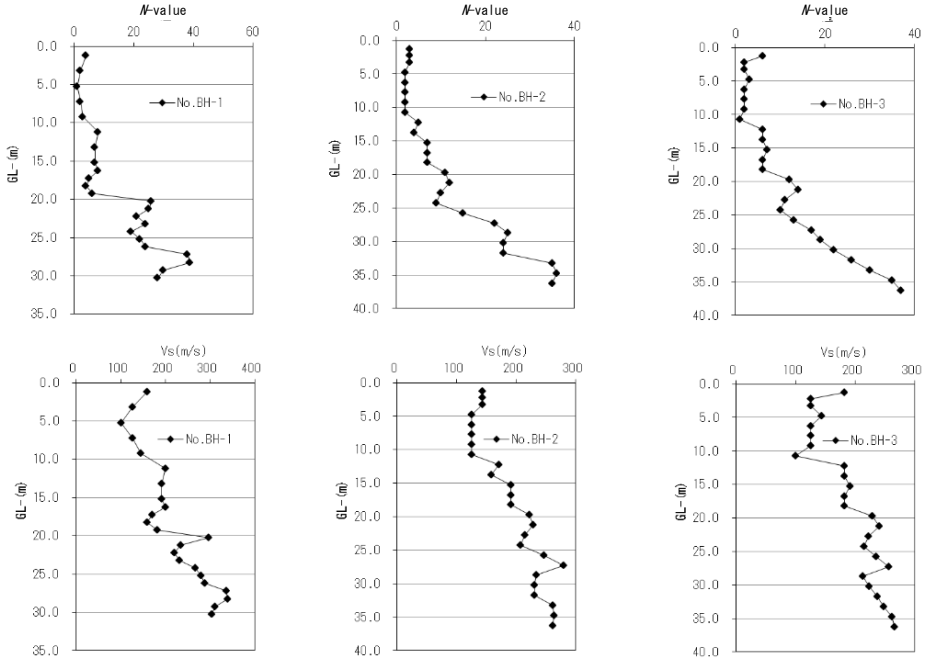

Fig. 7 *N*-value and *S*-wave velocity *V*s by SPT

Firstly, the *V*s profile up to GL−40 m was determined based on the boring data in Fig. 7 and shown by the red bold line in Fig. 8. Next, a geological structure that fits the *H*/*V* spectrum and the dispersion curve of the Rayleigh wave obtained through the micro-tremor was assumed as shown in Table 1 and Fig. 9. *V*s up to GL−40 m in Table 1 and Fig. 9 is the same as in Fig. 8. *P* wave velocity *V*p and mass density ρ was obtained by Eqs. (4) and (5) [18), 19)]. The geological structure between GL−40 m and GL−1230 m was determined by referring to the transfer function of SHAKE, the dispersion curve of the Rayleigh wave, *H*/*V* spectrum based on the diffuse wave field theory[20), 21), 22)], these will be discussed later in this paper, and the ground geological structure of YGNgro (Yangon University in Fig. 1) by Hirokawa et al.[23)]

$$V_{\mathrm{p}}(\mathrm{km/s}) = 1.29 + 1.1V_{\mathrm{s}}(\mathrm{km/s}) \tag{4}$$

$$\rho(\mathrm{t/m^3}) = 1.4 + 0.67\sqrt{V_{\mathrm{s}}(\mathrm{km/s})} \tag{5}$$

Table 1 Assumed underground structure

Depth (m)	Thickness (m)	Vs(m/s)	Vp (m/s)	ρ (t/m^3)	Poisson's Ratio
0m − 10m	10	120	1422	1.632	0.4964
10m −25m	15	200	1510	1.700	0.4911
25m −40m	15	300	1620	1.767	0.4822
40m −50m	10	400	1730	1.824	0.4718
50m −130m	80	520	1862	1.883	0.4577
130m −1230m	1100	1200	2610	2.134	0.3660
		3500	6030	2.653	0.2460

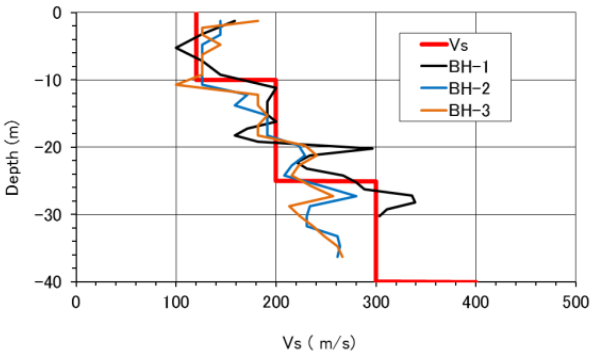

Fig. 8 *V*s up to GL−40m

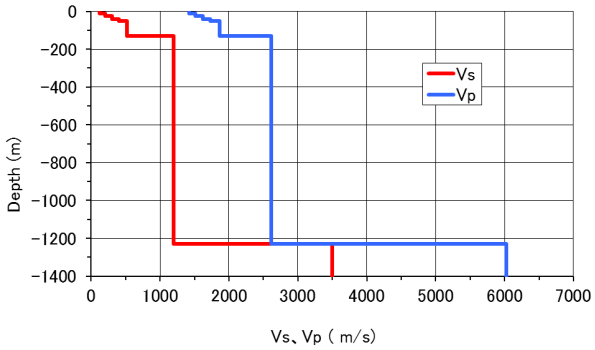

Fig. 9 Assumed underground structure

While the peak of *H*/*V* spectrum can be found at the long-period region of around 5 s also in the micro-tremor measurement by Hirokawa et al.[23)], they nevertheless set the engineering bedrock (*V*s = 1100 m/s) at the depth of 310 m with the following reasoning: "Regarding the peak observed around 0.2 Hz, […] while there is a high possibility that the frequency region below the first peak reflects the influence from an even deeper structure, it was excluded from the area of examination of this study because there is not sufficient information determining the structure due to it being outside the observable frequency region of array." Meanwhile, the model in Fig. 9 assumed a geological structure with seismic bedrock (*V*s = 3500 m/s) at the depth of 1230 m in order to represent the peak at long-period region seen in the *H*/*V* spectrum.

4.2 Transfer function of SHAKE

Nakamura[24] claimed that the *H*/*V* spectrum of micro-tremor could approximately represent the *S*-wave amplification characteristics of the surface subsoil during an earthquake. In other words, it was claimed that it could represent both the dominant frequency and the amplification factor of the ground. For this reason, it is important to compare the transfer function of SHAKE[25] based on the multiple reflection theory of *S*-wave (Eq. (6)) and the *H*/*V* spectrum of micro-tremor.

$$T(\omega) = \frac{E(\omega) + F(\omega)}{2E_0(\omega)} \tag{6}$$

Here, $E(\omega)$ and $F(\omega)$ are the incident wave and reflection wave at the ground surface respectively, and $E_0(\omega)$ is the incident wave to the surface of seismic bedrock.

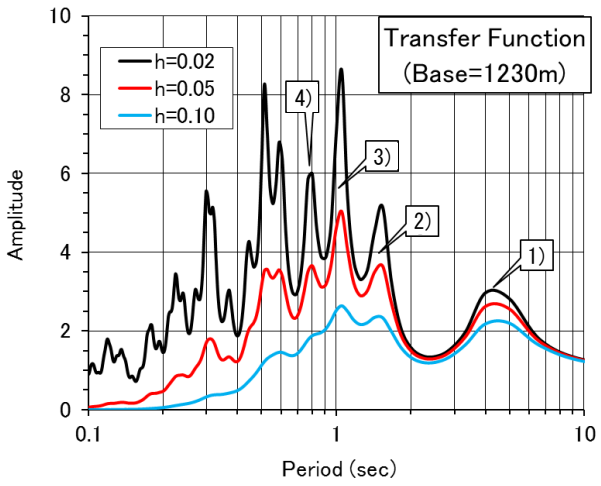

Fig. 10 Transfer function of SHAKE (*h*=2%, 5%, 10%)

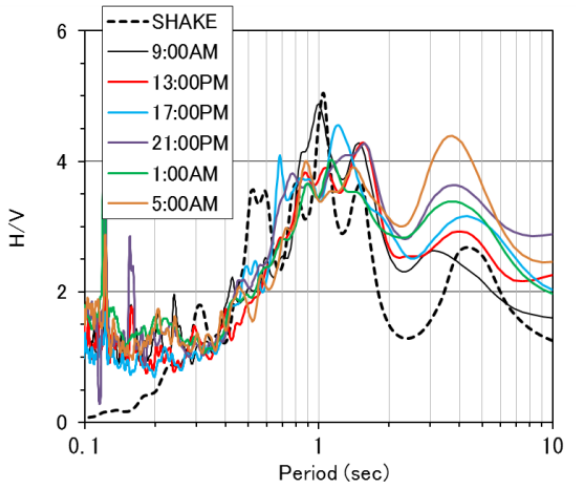

Fig. 11 Transfer function of SHAKE (*h*=5%)) and *H*/*V* of micro-tremor

Figure 10 shows the transfer function of *S*-wave that used the *V*s profile in Table 1. It shows the results for when the damping ratio was h = 2%, 5% or 10%, and the peaks from 1) to 4) in the graph corresponded to the first to fourth shear modes (The details of these modes are discussed later in Fig.20).

Figure 11 shows a comparison between the transfer function with h = 5% and the *H*/*V* spectrum shown in Fig. 4. The peak in the long period around 4 s, and several peaks around 1 s are expressed to some extent.

4.3 Rayleigh wave theoretical dispersion curve and *H*/*V* spectrum

Figure 12 shows the dispersion curve of the phase velocity of the Rayleigh wave using the geological structure in Fig. 9. A part of the theoretical seismic motion calculation program (phs3a.f) by Hisada[26] was used to calculate the four full lines in the graph. Moreover, the method of Lysmer[27), 28), 29)] was used to calculate the marks including circles, squares and triangles. As the method of Lysmer is FEM, to represent semi-infinite ground, a base layer that is 1.5 times thicker than the wavelength of the *S*-wave was added for each period deeper than the surface of seismic bedrock. The two are almost the same, and Figs. 5 and 6, shown earlier, include the theoretical dispersion curves for their fundamental mode (the lowest mode).

In Fig. 12, *P1* mode (M_{11} mode[30]) defined by Lysmer[27] intersects with *S1* mode (M_{21} mode[30]) at

around 2.4 s. For the period region shorter than 2.4 s, *P1* mode is the fundamental mode, and *S1* mode is the fundamental mode for the period region longer than that. Figure 13 shows the *H*/*V* spectrum (absolute value) of fundamental mode and first higher mode. The black circle in the graph indicates the intersection (2.4 s, *H*/*V*=1) of the modes. The horizontal component becomes highly prominent in the fundamental mode at 3.2 s that is close to the first natural period of the *S*-wave shown in Fig. 10. Figure 14(a) shows the fundamental mode shape at 3.2 s, possessing the strong characteristics of the primary shear deformation mode (*S1* mode). The minimum of *H*/*V* spectrum, which is the peak of *V*/*H* spectrum, appears in the first higher mode at 2.56 s. The mode shape of this first higher mode at 2.56 s is as shown in Fig. 14(b), and it possesses the characteristics of the vertical first mode (*P1* mode) of the entire ground. Appendix 2 describes the dispersion curve of the one-layer fixed bottom (rigid basement) model and the two-layer semi-infinite ground where the mode shape is clearly identified. Similarly to Fig. 12, this model also shows an intersection of modes, namely *P1* mode being the fundamental mode of short-period region and *S1* mode being the fundamental mode of long-period region.

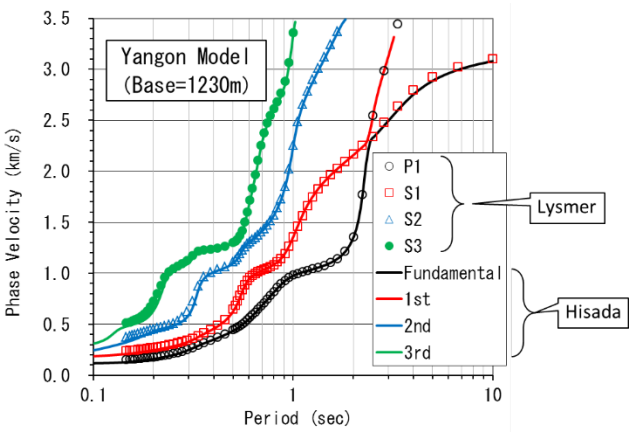

Fig. 12 Theoretical dispersion curve of Rayleigh wave

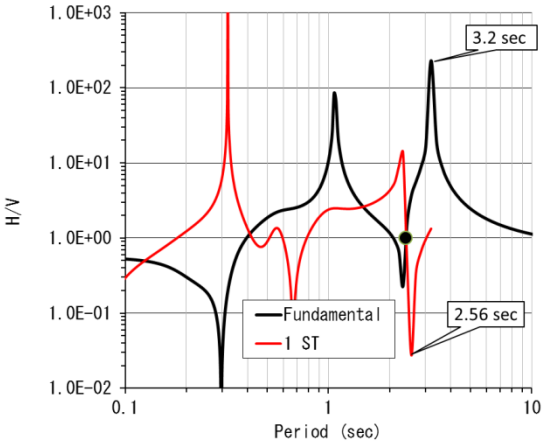

Fig. 13 *H*/*V* of the Rayleigh wave mode

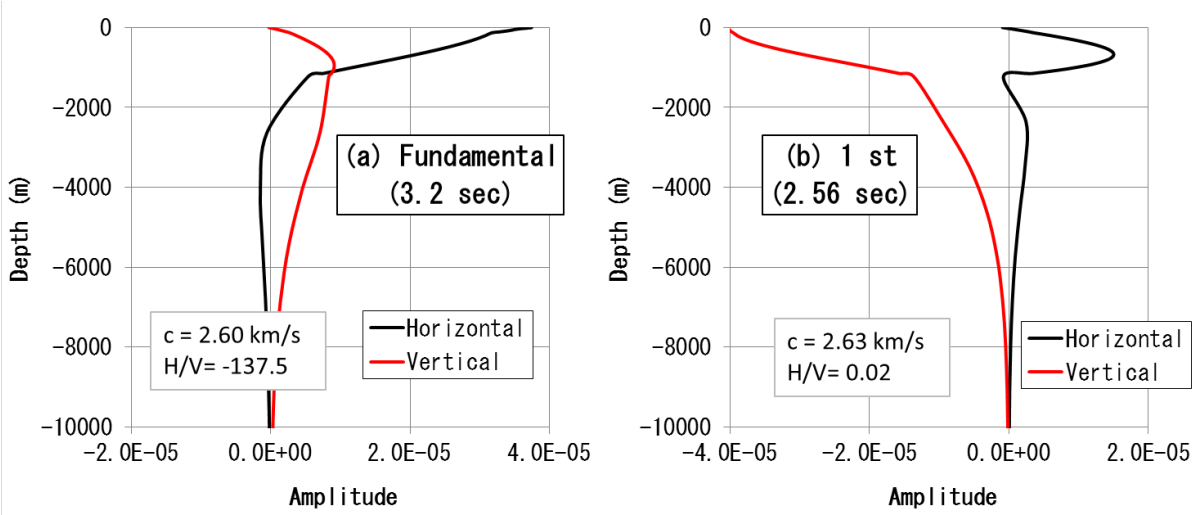

Fig. 14 Fundamental mode at 3.2 s and first higher mode at 2.56 s

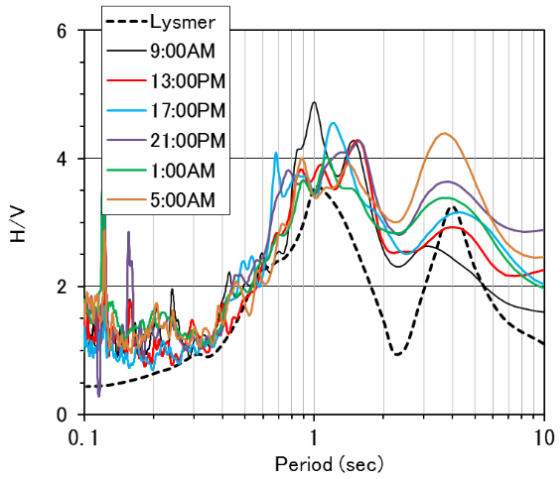

Fig. 15 *H*/*V* of Rayleigh wave obtained by the method of Lysmer and *H*/*V* of micro-tremor

The following equation expresses the *H*/*V* spectrum of the Rayleigh wave obtained by using the normalized eigenfunction defined by Lysmer[28] (see Appendix 3), and Fig. 15 shows its comparison with the *H*/*V* of micro-tremor (Fig. 4).

$$\left(\frac{H}{V}\right)_{\text{Lysmer}} = \frac{\sqrt{\sum_{m=0}^{M}(R_{\text{H}m})^2}}{\sqrt{\sum_{m=0}^{M}(R_{\text{V}m})^2}} \tag{7}$$

Here, $R_{\text{H}m}$ is the horizontal amplitude at the mth-order mode of the Rayleigh wave, and $R_{\text{V}m}$ is similarly the vertical amplitude at the mth-order mode. They enable amplitude comparison between modes. They are both complex numbers, and their real part is used for $R_{\text{H}m}$, and their imaginary part is used for $R_{\text{V}m}$. M represents the total number of all modes that exist in that frequency, and Fig. 15 shows the results for $M = 4$ (fundamental mode, first to fourth higher modes). For instance, the cut off period of the first higher mode in Fig. 12 is 3.2 s. For Fig. 15, the so-called normal mode up to the cut off period and the complex number mode[28), 29)] that appears ahead of this normal mode was outputted. Similarly to Fig. 11 that used SHAKE, Fig. 15 well represents the peaks around 4 s and 1 s. However, while there were several peaks around 1 s in Fig. 11, only one peak is observed in Fig. 15.

4.4 *H*/*V* spectrum based on the diffuse wave field theory

According to the diffuse wave field theory of Sanchez-Sesma et al.[20], the *H*/*V* spectrum of micro-tremors at an arbitrary point on the ground surface, which is a three-dimensional elastic body, can be represented by the ratio of the imaginary part of the Green function whose excitation point and receiving point are both that same point. Since this theory can also be applied to an irregular three-dimensional ground, there are several examples of analysis using three-dimensional FEM, and a program[21), 22)] has been released for the theoretical solution of horizontal one-dimensional problem. Figure 16 shows the comparison between the *H*/*V* spectrum obtained by the diffuse wave field theory and the *H*/*V* spectrum of micro-tremor (Fig.4). While Fig. 4 of Reference 20) includes the comparison between the case where damping is $Q = 100$ and $Q = \infty$ (undamped), the released program only includes the case where $Q = \infty$ (undamped), and for the result shown in Fig.16 may also be $Q = \infty$ (undamped).

Similarly, to Fig. 11 that used SHAKE and Fig. 15 that used Lysmer, Fig. 16 well represents the peaks around 4 s and 1 s. And similar to Fig.15, only one peak around 1 s is observed in Fig. 16.

Figure 17 compares the transfer function obtained by SHAKE, the *H*/*V* spectrum obtained by Eq. (7) of Lysmer and the *H*/*V* spectrum obtained by the diffuse wave field theory. The peak and trough periods of the three theoretical *H*/*V* spectrums mostly coincide with each other. The reason for the peak amplitude of the one by diffuse wave field theory being high is inferred to be the influence of it being

undamped ($Q = \infty$). This is because this theory employs full wave field and therefore includes the contributions from body waves (S_H wave, S_V wave and P wave) and surface waves (Rayleigh wave and Love wave), and the amplitude of the body waves is strongly influenced by attenuation. Thus, considering the fact that the H/V spectrum of the transfer function obtained by SHAKE and that of micro-tremor mostly coincide, this ground is inferred to be a ground where the body wave is predominate. The reason why the H/V spectrum obtained by Eq. (7) of Lysmer and that of micro-tremor coincide is because the so-called normal mode and the complex mode[28), 29)] were added, meaning that this process evaluates the contributions of the body waves and the so-called leaking modes[30)].

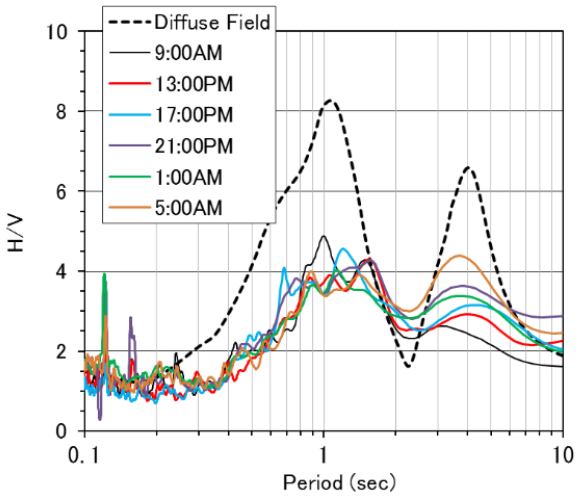

Fig. 16 H/V spectrum based on the diffuse wave field theory

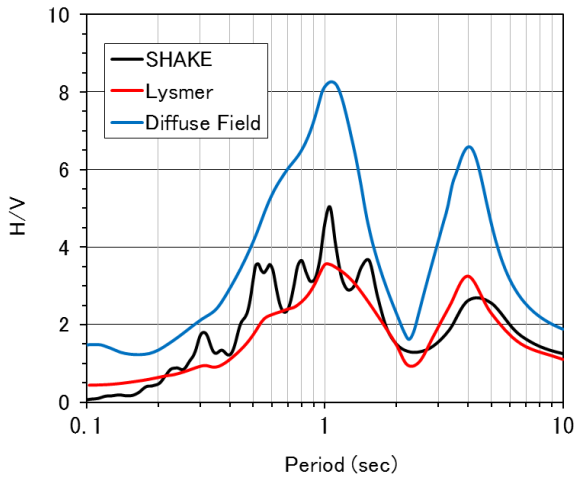

Fig. 17 H/V spectrum based on three theories

5. COMPARISON WITH THE GEOLOGICAL STRUCTURE IN BANGKOK

One of the authors of this paper has estimated a geological structure of Bangkok using the H/V spectrum of micro-tremor focused on microseisms similar to this study[5)]. Bangkok is located approx. 610 km southeast of Yangon. It is built at the mouth of Chao Phraya river, and, geological structure is thought to be similar to Yangon.

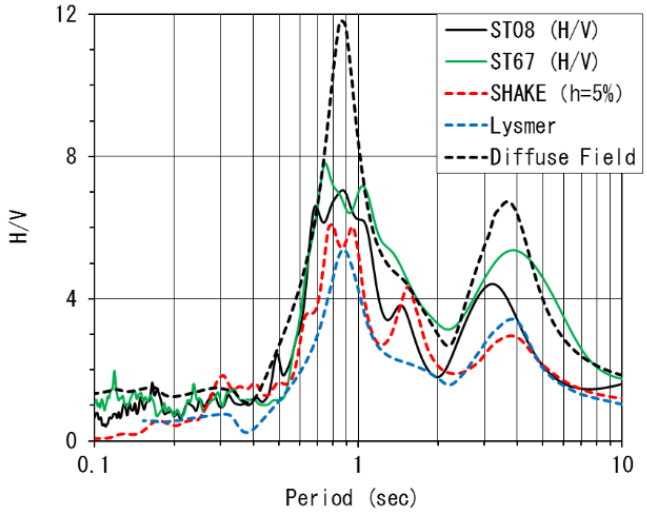

Fig. 18 H/V spectrum of the ground of Bangkok

Table 2 Underground structure of the ground of Bangkok

Depth (m)	Vs(m/s)	Vp (m/s)	ρ (t/m3)
0m – 7m	60	300	1.70
7m – 15m	80	300	1.70
15m – 30m	290	800	1.85
30m – 60m	350	800	1.90
60m – 120m	410	900	1.90
120m – 240m	550	1100	2.00
240m – 720m	770	1500	2.10
	2000	3800	2.35

Figure 18 compares the *H*/*V* spectrum of micro-tremor obtained from two typical measurement points (ST08 and ST67), transfer function of *S*-wave obtained by SHAKE using the estimated underground structure (Table 2) and the *H*/*V* obtained by Eq. (7) of Lysmer (Figs. 5 and 7 of Reference 5)). The *H*/*V* spectrum obtained by the diffuse wave field theory ($Q=\infty$) was newly added to it.

Similarly, to Fig. 11 of this study, two large peaks at the long-period region of around 4 s, and around 1 s, were also recorded at the ground of Bangkok, and SHAKE, Eq. (7) of Lysmer and diffuse wave field theory all represent both peak periods well. The peak around 4 s reflects the dynamic characteristic of the entire ground up to the depth of 720 m, and the peak around 1 s reflects the dynamic characteristic of the extremely weak Bangkok Clay layer (the colored section in Table 2), whose $Vs<$ 100 m/s and stratum thickness is 15 m. Figure 19 shows the shear deformation modes of SHAKE at 4 s and 0.8 s in Fig. 18. This figure expresses the transfer function at each ground depth ($E(\omega)$ and $F(\omega)$ of Eq. (6) are respectively set as the upward transmitting wave and the downward transmitting wave at each depth), and, similarly to the eigenmode that takes the participation coefficient in modal analysis into account (so-called participation function), it enables comparison of amplitude between modes. 4 s is the primary mode of the entire 720 m deep ground, and 0.8 s is the mode where the third mode of the entire ground became coupled with the primary mode of the surface subsoil, and one can see that the primary mode of the weak surface subsoil is highly prominent.

Meanwhile, though Fig. 11 of the ground of Yangon shows the peak at the long-period region of around 4 s also several peaks around 1 s, it does not possess extremely weak surface subsoil, unlike the ground of Bangkok. Figure 20 shows the first to the fourth shear deformation modes shown in Fig. 10. In Fig. 10, 1.05 s of ③ and 0.80 s of ④ are the modes where the third mode and the fourth mode of the entire ground respectively became coupled with the primary mode of the surface subsoil (up to GL−130 m). While the deformation of the surface subsoil is prominent, it is not as much as the deformation at 0.8 s in Fig. 19.

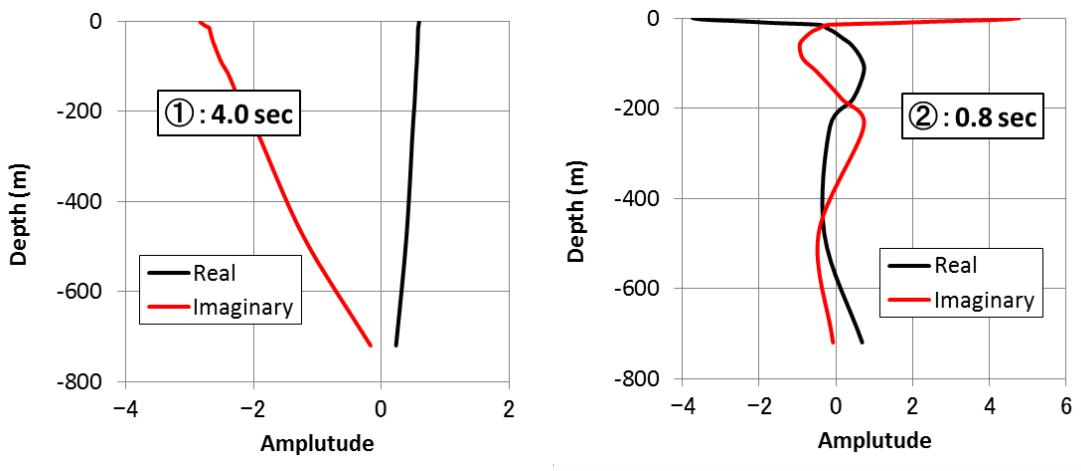

Fig. 19 Shear deformation mode of the ground of Bangkok (*h*=5%)

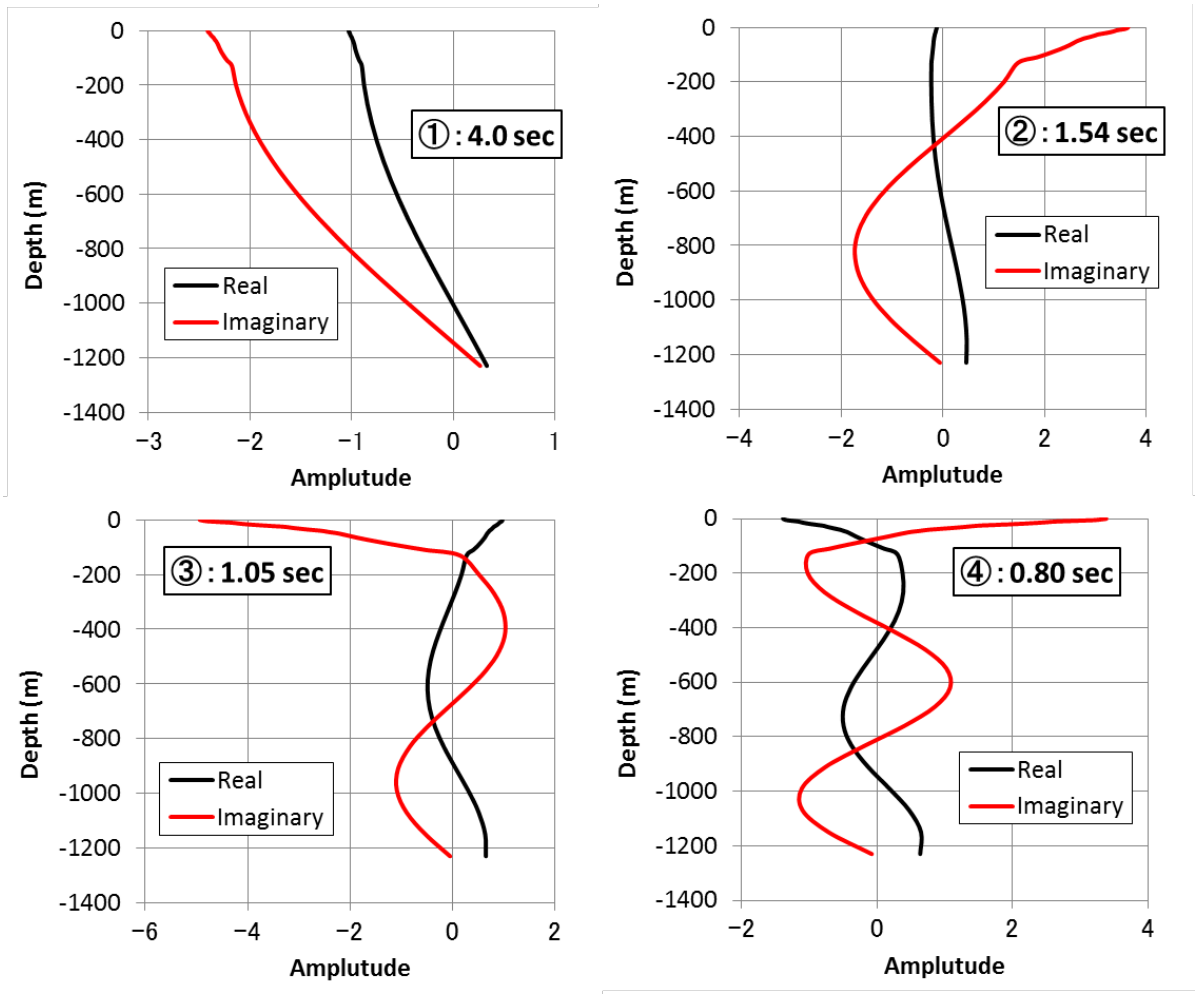

Fig. 20 The first to the fourth shear deformation mode of the ground of Yangon (h=5%)

6. CONCLUSION

Currently, no data or information on the geological structure under Yangon City is available. For this reason, this study conducted micro-tremor measurement focusing on long-period micro-tremor (microseisms) and estimated an initial model as a first step toward the examination of the deep geological structure under Yangon City. However, the trustworthiness of this model is not yet perfect. Moreover, the reason why the observation H/V spectrum from the dry season shows only one peak around 1 s while that of the rainy season shows several peaks between 0.8 s to 1.5 s in addition to the peak in long-period region of 3 s to 5 s is yet to be investigated further. An array observation that will reflect the deeper structure is planned for the future. The record of this observation will be used to validate and obtain more accurate picture of the geological structure. In addition, the monthly changes of H/V spectrum are being conducted, and we are simultaneously recording the wind velocity and significant wave heights at four points on the Andaman Sea. We would like to examine the relationship between the occurrence of long-period micro-tremor (microseisms) and the meteorological conditions such as significant wave height based on this result.

In the future, Stochastic Green function from the seismic motion whose hypocenter is the Sagaing fault or the subduction structure of the Andaman Sea will be predicted at the surface of seismic bedrock, and strong motion simulations will be conducted by multiplying the amplification characteristics of the estimated ground geological structure.

ACKNOWLEDGEMENT

This study used the micro-tremor analysis program Bido 2.0[12] by Dr. Ikuo Cho of the National Institute of Advanced Industrial Science and Technology, the program based on the diffuse wave field theory by Professor Sanchez-Sesma et al. [21] of the National Autonomous University of Mexico (UNAM), the theoretical seismic motion calculation program[26] by Professor Yoshiaki Hisada of Kogakuin University, and Bessel function[31] by Assistant Professor Takuya Oura of Kyoto University's Research Institute for Mathematical Sciences, among others. We express our gratitude.

APPENDIX 1

Appendix Fig. 1(a) compares the dispersion curve obtained by BIDO 2.0[12] (SPAC method) and the dispersion curve obtained by SPAC method program developed for this study. Moreover, Appendix Fig. 1(b) compares the results when CCA method was used instead by the two programs. Artificially synthesized data for demonstration (R=18m)[12] was used as the waveform data, FORTRAN function (dbesj0(X) and dbesj1(X)) released by Oura[31] was used as the Zero-order Bessel function of the first kind and the First-order Bessel function of the first kind, respectively. Inverse transformation of the Zero-order Bessel function for SPAC method was conducted up to the first zero cross position (argument X=2.41). When using BIDO 2.0[12], the original waveform was divided by the length of segment (20.48 s) and smoothed by Parzen window (bandwidth 0.3 Hz) after removing the trend of each segment and applying COS type taper on them in order to obtain the average of 10 segments. The segment to be used is selected automatically from the RMS of each segment. Therefore, the program developed for this study has a different range of data and preprocessing method. However, largely similar dispersion curves were obtained from them at between 0.1 s and 10 s.

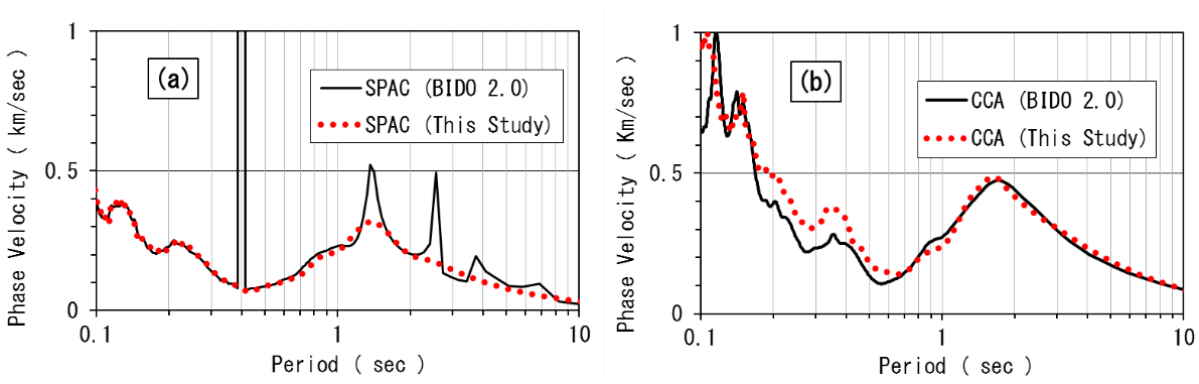

Appendix Fig. 1 Comparison between the analysis result of BIDO 2.0 and that of this study

APPENDIX 2

Appendix Fig. 2 shows the dispersion curves of the phase velocity and group velocity of the one-layer fixed bottom (rigid basement) model. The thickness of the surface subsoil is H = 10 m, Vs = 100 m, mass density ρ = 1.8 t/m^3, and Poisson's ratio v = 0.25 (Vp = 173.2 m/s). At 2.5Hz and 7.5Hz, which are the natural frequencies of S-wave, phase velocity ∞ and zero group velocity of *S1* mode and *S2* mode appear. At 4.33Hz, which are the natural frequency of P wave, phase velocity ∞ and zero group velocity of *P1* mode appear. Namely, body waves are defined as surface waves with infinite wavelength[30].

Appendix Fig. 3 shows the dispersion curve of two-layer semi-infinite ground model. The physical properties of the surface subsoil are the same as those of Appendix Fig. 2, and it show the case of when basement stratum is ρ = 2.0 t/m^3, Vs = 500 m/s and Vp = 1500 m/s. Its fundamental mode becomes asymptotic to phase velocity c = 474 m/s when frequency is zero. This characteristic where *S1* mode

becomes the fundamental mode when in low frequency region and *P1* becomes the fundamental mode when in high frequency region is akin to that of Fig. 12. Since the *H*/*V* spectrum (ellipticity) on the ground surface differs depending on whether the fundamental mode is *S1* mode or *P1* mode, identification of the mode is important.

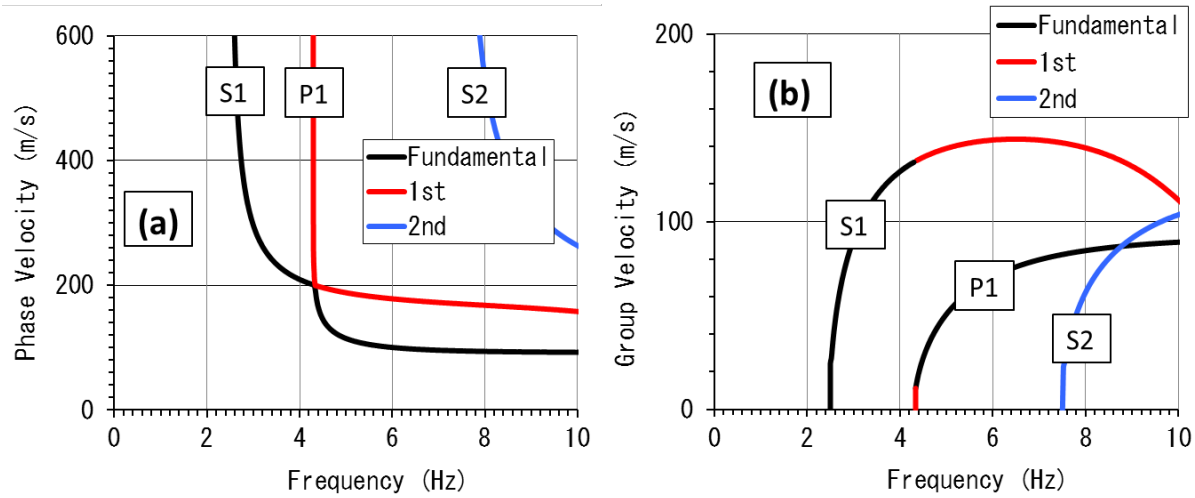

Appendix Fig. 2 Dispersion curve of one-layer fixed bottom (rigid basement) model

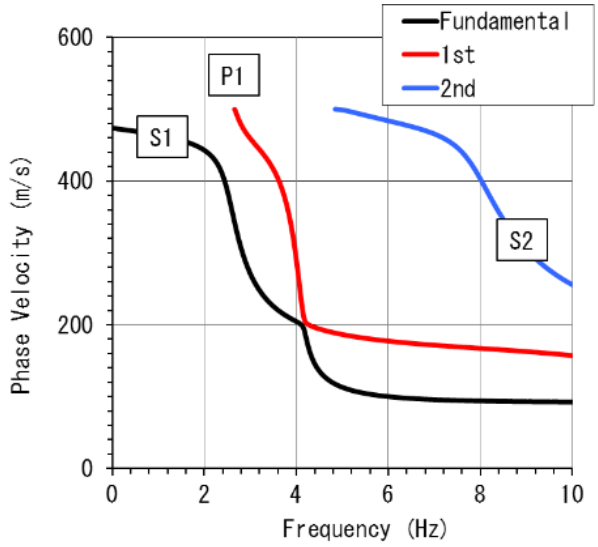

Appendix Fig. 3 Dispersion curve of two-layer semi-infinite ground model

APPENDIX 3

In the method of Lysmer[27), 28), 29)], eigenvalue (wavenumber k_s) and eigenvector $\{V\}_s$ at angular frequency ω from a simple eigenvalue analysis can be obtained without using the displacement potential. $\{V\}_s$ is normalized by the following equation.

$$\{V^*\}_s{}^T\{[A]k_s{}^2-([G]-\omega^2[M])\}\{V\}_s=2k_s{}^2 \quad s=1,2\cdot\cdot\cdot\cdot 2n \qquad \text{Appendix Eq. (1)}$$

Here, $[A]$ and $[G]$ are the stiffness matrixes, $[M]$ is the mass matrix, n is the vertical direction

partitioned element number, and $\{V^*\}_s$ is conjugate vector of $\{V\}_s$. Therefore, the eigenmode $\{V\}_s$ at each frequency enables amplitude comparison between each mode, similarly to Fig. 19 and Fig. 20 of SHAKE. Moreover, the group velocity *Us* of the real number mode can be expressed in the following equation using this $\{V\}_s$, and it does not require numerical differentiation.

$$U_s = \frac{d\omega}{dk_s} = \frac{k_s/\omega}{\{V^*\}_s{}^T[M]\{V\}_s} \qquad \text{Appendix Eq. (2)}$$

REFERENCES

1) InterRisk Asia Thailand: Earthquake Risk in Myanmar, *InterRisk Thailand News*, No. 7, pp. 1–10, 2015. (in Japanese)
2) Yoneura, D., Takamiya, K., Kaneko, T., Yamada, Y. and Morio, S.: Micro-tremor Observation in Yangon City Evaluating Micro-seisms, *51st Proceedings of the Japan conference on Geotechnical Engineering*, pp. 1651–1652, 2016. (in Japanese)
3) Hello Happy Life: *Map of Yangon Township*, http://livedoor.blogimg.jp/hellohappylife/imgs/8/a/8a31029f.jpg (last accessed on 2020).
4) Murakami, H., Tsuchida, T., Yamada, Y. and Aoyama, T.: Consideration of Physical and Mechanical Characteristics of Clayey Soils in Myanmar, *Japanese Geotechnical Journal*, Vol. 10, No. 1, pp. 163–172, 2015. (in Japanese)
5) Morio, S., Kato, Y., Kitazumi, A. and Koswan, S.: Estimation of the Deep Underground Soil Structure in Bangkok Metropolitan Area through Micro-tremor Observation, *Japanese Geotechnical Society*, Vol. 60, No. 9, pp. 24–27, 2012. (in Japanese)
6) Okano, K.: Observational Study on Microseisms (Part 1), *Bulletins Disaster Prevention Research Institute*, Kyoto University, No. 44, 1961.
7) Okano, K.: Observational Study on Microseisms (Part 2), *Bulletins Disaster Prevention Research Institute*, Kyoto University, No. 47, 1961.
8) Sato, H.: Easy Geophysical Exploration, *Geophysical Exploration News*, The Society of Exploration Geophysicists of Japan, pp. 1–4, 2014. (in Japanese)
9) Obara, K.: Yearly change of noise level and detection capability of microearthquakes for NIED-Hi-net, Abstracts, *Japan Earth and Planetary Science Joint Meeting*, S045-P009, 2001. (in Japanese)
10) Cho, I., Tada, T. and Shinozaki, Y.: A New Method of Micro-tremor Exploration Using Miniature Seismic Arrays: Quick Estimation of Average Shear Velocities of Shallow Soil, *Geophysical Exploration*, Vol.61, No.6, pp.457–468, 2008. (in Japanese)
11) Cho, I., Tada, T. and Shinozaki, Y.: Centerless circular array method: Inferring phase velocity of Rayleigh waves in broad wavelength ranges using micro-tremor records, *Journal of Geophysical Research*, Vol. 111, No. 9, B09315, doi:10.1029/2005JB004235, 2006.
12) National Institute of Advanced Industrial Science and Technology: BIDO Version2.0, 2010. https://staff.aist.go.jp/ikuo-chou/BIDO/2.0/bido_manual2.0.pdf. (last accessed on 2017-12-05)
13) Chavez-Garcia, J. F., Rodriguez, M. and Stephenson, R. W.: Subsoil Structure Using SPAC Measurements along a Line, *Bulletin of Seismological Society of America*, Vol. 96, No. 2, pp. 729–736, 2006.
14) Konno, K.: Theoretical Study on the Spatial Auto-correlation Method for Estimation of Underground Structure using Microtremor, *Journal of Japan Society of Civil Engineering*, No. 654/I-52, pp. 367–375, 2007. (in Japanese)
15) Yokoi, T. and Margaryan, S.: Re-checking Spatial Auto Correlation method based on the theory of seismic interferometry, *Geophysical Exploration*, Vol.61, No.2, pp.87–99, 2008. (in Japanese)
16) Morikawa, H., Ohori, M. and Iiyama, K.: A Study on Stochastic Properties of Auto-Correlation Coefficients for Microtremor Data Simultaneously Observed at Two Sites, *Journal of Japan Association for Earthquake Engineering*, Vol.10, No.2, pp. 89–106, 2010. (in Japanese)
17) Japan Road Association: Specifications for Highway Bridges—Part Ⅴ Seismic Design, Japan Road Association, 2012. (in Japanese)

18) Kitsunezaki, C., Goto, N., Kobayashi, Y., Ikawa, T., Horike, M., Saito, T., Kurota, T., Yamane, K. and Okuzumi, K.: Estimation of P- and *S*-wave Velocities in Deep Soil Deposits for Evaluating Ground Vibrations in Earthquake, *Natural Disaster Science*, Vol. 9, No. 3, pp. 1–17, 1990. (in Japanese)
19) Ota, T., Emori, K. and Kasai, Y.: *Earthquake Resistance/Vibration/Control*, Kyoritsu Shuppan, 339 p., 2001. (in Japanese)
20) Sanchez-Sesma, F. J., Rodriguez, M., Iturraran-Viveros, U., Luzon, F., Campillo, M., Margerin, L., Garcia-Jerez, A., Suarez, M., Santoyo, M. A. and Rodriguez-Castellanos, A.: A theory for micro-tremor *H*/*V* spectral ratio: application for a layered medium, *Geophysical Journal International*, Vol. 186, No. 1 , pp. 221–225, 2011.
21) Garcia-Jerez, A., Sanchez-Sesma, F. J., Luzon, F. and Perton, M.: A computer code for forward calculation and inversion of the *H*/*V* spectral ratio under the diffuse field assumption, *Computer & Geoscience*, Vol. 97, pp. 67–78, 2016.
22) García-Jerez, A. and Piña-Flores, J.: *H*/*V-Inv 1.0—A software for inversion of H/V spectral ratios of ambient noise based on the Diffuse Field Approximation*, https://w3.ual.es/GruposInv/hv-inv/. (last accessed on 2020)
23) Hirokawa, Y., Matsuhima, S., Kawase, H., Naing, T. and Thant, M.: Estimation of underground structures in Yangon City, Myanmar using single-station and array microtremors, *Journal of Japan Association for Earthquake Engineering*, Vol.16, No.1, pp. 49–58, 2016. (in Japanese)
24) Nakamura, Y.: A method for dynamic characteristics estimation of subsurface using micro-tremor on the ground surface, *Quarterly Report of Railway Technical Research Institute*, Vol. 30, No. 1, pp. 25–33, 1989.
25) Schnabel, P. B., Lysmer, J. and Seed, H. B.: SHAKE—A Computer Program for Earthquake Response Analysis of Horizontally Layered Sites, Report No. EERC 72–12, 1972.
26) Hisada, Y.: Efficient Methods for Computing Green's Functions and Normal Mode Solutions for Layered Half-spaces, *Journal of Structural and Construction Engineering*, Architectural Institute of Japan, No. 501, pp. 49–56, 1997. (in Japanese)
27) Lysmer, J.: Lumped mass method for Rayleigh waves, *Bulletin of the Seismological Society of America*, Vol. 60, No. 1, pp. 89–104, 1970.
28) Lysmer, J. and Drake, L. A.: A Finite Element Method for Seismology Method in Seismological Physics, *Seismology—Surface Waves and Earth Oscillations*, Academic Press, Chap. 4, pp. 181–216, 1973.
29) Morio, S. and Kato, Y.: Complex Eigenvalue Analyses of Love and Rayleigh Waves, *Proceedings of the 28th JSCE Earthquake Engineering Symposium*, Seismic motion/Ground property (048), pp. 1–6, 2005. (in Japanese)
30) Tajime, K.: Story of Surface Wave, *Geophysical Exploration*, Vol. 36, No. 1, pp. 23–32, 1983. (in Japanese)
31) Oura, T.: Bessel Function—Integer Order, Research Institute for Mathematical Sciences, Kyoto University, http://www.kurims.kyoto-u.ac.jp/~ooura/bessel-j.html. (last accessed on 2020)

(Original Japanese Paper Published: February, 2019)
(English Version Submitted: December 3, 2019)
(English Version Accepted: February 28, 2020)